Applied Physics A (2026) 132:716
https://doi.org/10.1007/s00339-026-09906-3

Applied Physics A
Materials Science & Processing

Investigation of synergistic effect of microwave assisted MoO_3 loaded V_2O_5 nanocomposites for electrochemical supercapacitor

K. Latha[1] **· S. Anbuselvi**[2]

Received: 2 April 2026 / Accepted: 3 July 2026
© The Author(s), under exclusive licence to Springer-Verlag GmbH Germany, part of Springer Nature 2026

Abstract
A series of microwave-assisted MoO_3 loaded V_2O_5 nanocomposites was prepared and tested as electrochemical supercapacitor electrode material. The novelty of the study is that the MoO_3/V_2O_5 heterostructured nanocomposites have been fabricated in a very short time using microwave radiation and their synergistic electrochemical activity in acidic and alkaline electrolytes investigated. The structural studies confirmed the presence of both V_2O_5 and MoO_3, and the FESEM studies showed that the morphology of powder changes from a lamellar sheet to a nanorod-like shape when MoO_3 is added to V_2O_5. The electrochemical performance of the prepared samples were studied for the nanocomposite of MoO_3 loaded on V_2O_5 with specific capacitances of 224 F g^{-1} and 172 F g^{-1}, respectively, in 1 M H_2SO_4 and 3.5 M KOH electrolytes at 1 A g^{-1}. The synergic effect of MoO_3 and V_2O_5 gives better performance due to better charge transfer and ion diffusion. The optimized electrode showed good electrochemical stability with 71% capacitance remaining after 5000 charge-discharge cycles. In addition, energy density and power density values were estimated and presented for the synthesized nanocomposites, which demonstrated the prospects of the nanocomposites in the field of electrochemical energy storage.

Keywords Supercapacitor · Hybrid nanocomposites · V_2O_5 · Microwave-assisted method

1 Introduction

Rapid development of electronics, electric vehicles, wearable devices and renewable energy systems has resulted in a need for efficient and sustainable energy storage solutions. Even though the fossil fuels are still the primary source of energy in the world, worries about environmental pollution, climate change and resource depletion have led to the rapid development of clean and renewable energy sources. Solar and wind energy are intermittent, however, and require the use of sophisticated energy storage devices that are able to store and release energy efficiently [1]. Conventional dielectric capacitors, batteries and electrochemical supercapacitors have garnered considerable interest among the different energy storage technologies. The typical battery has a high energy density, but a low power density and relatively slow charge/discharge rate. Conventional capacitors however have high power density, but very low energy storage ability [2]. Extensive scientific research has been dedicated to studying supercapacitors, which are alternatively called electrochemical or ultracapacitors. These capacitors are employed with lithium-ion batteries due to their exceptional power density, rapid charge and discharge capabilities, and prolonged operational lifespan [1, 2]. On the other hand, supercapacitors have a very low energy density, which makes it difficult for them to be used independently as standalone devices [3, 4]. The specific capacity of active material has to be enhanced through a practical approach to developing supercapacitors with a higher energy density. In general, high-capacitance electrode materials have both a large surface area and a high electrical conductivity rate since these characteristics are intimately connected to the electroactive surface for redox reactions, resulting in pseudocapacitance across the electrode materials [5, 6].

Numerous carbonaceous materials with a large surface area are still used to produce supercapacitors' electrode materials [7]. Some examples of these materials are

✉ K. Latha
drlatha.chem@gmail.com

[1] Department of Chemistry, Vivekanandha College of Engineering for Women (Autonomous), Tiruchengode, Namakkal-Dt, Tamil Nadu 637205, India

[2] Department of Chemistry, Sri Sarada College for Women (Autonomous), Salem-Dt, Tamil Nadu 636016, India

Published online: 08 July 2026

graphene, activated carbon, and carbon nanotubes [8]. When subjected to rapid charging and discharging, the capacitance of these carbon-based electrochemical double-layer capacitors drops dramatically. Metal oxides, nitrides, and hydroxides encounter certain shortcomings of carbon, which typically display high capacitance for energy storage due to the more cost-effective storage mechanism they adopt [9]. Furthermore, metal oxides and hydroxides have the potential to serve as the active materials of supercapacitors that have a comprehensive energy density. V_2O_5 is thought to be one of the most suitable alternatives among many owing to its high energy density, wide availability, relatively inexpensive, one-of-a-kind layered structure, blended oxidation states (V^{2+}, V^{3+}, V^{4+}, and V^{5+}), and it has a simple synthesizing method [10, 11].

In addition, it possesses a unique layered structure. Several forms of active material based on V_2O_5 have been identified for supercapacitors. The advancement in the capacity of supercapacitors is possible through the implementation of two primary strategies. The first strategy involves decreasing the size of the V_2O_5 substances to the nano size [12, 13]. This is done because nanomaterials have a substantial surface area and small diffusion spaces, which can offer additional electrochemically active sites and facilitate the concentration polarization of active material. When compared with non-nanostructured materials, various types of V_2O_5 nanostructures [14], such as nanowires, nanosheets, nanofibers, nanorods, and hollow microcapsules, are effective in enhancing electrochemical kinetics and lowering the diffusion distance for Li+ ions. These nanostructures have been proven efficient in improving electrochemical kinetics [1, 15, 16].

Incorporating highly conductive substances into V_2O_5 should be considered the second strategy for enhancing the capacity of supercapacitors. This is because conductive materials may significantly increase the rate at which electronic transfer occurs [17]. In earlier research, several different kinds of conductive materials, such as carbon nanotubes (CNT), mesoporous carbon, graphene, and conductive polymer, were examined as possible supports for developing V_2O_5-based nanostructured materials.

While V_2O_5-based hybrid nanocomposites, like WO_3/V_2O_5 and MnO_2/V_2O_5, have been explored earlier for electrochemical energy-storage applications, the effects of MoO_3 incorporation into V_2O_5 have been comparatively less investigated. The comparative table illustrating the performance was provided in Table 1. MoO_3 has a high theoretical capacitance, a number of oxidation states and can be proton-intercalated with good proton-intercalation ability, thus offering additional redox-active sites and improving charge-transfer processes. Moreover, heterointerfaces of MoO_3/V_2O_5 are expected to enhance electron transport and ion diffusion kinetics. This makes it worth studying the synergistic effect between MoO_3 and V_2O_5 with microwave-assisted synthesis reactions to gain insight into structure-property relationships and enhance the performance of supercapacitors.

2 Experimental methods

2.1 Preparation of MoO_3/V_2O_5 nanocomposites

The synthesis of MoO_3/V_2O_5 nanocomposites was accomplished through the following procedure: Separate solutions of 0.1 M ammonium metavanadate (NH_4VO_3) and 0.1 M ammonium molybdate ($(NH_4)_6Mo_7O_{24}$) were prepared. The pH levels of these solutions were then adjusted to approximately 2 by gradually adding HNO_3 solution while maintaining continuous stirring. Following a designated period, solutions containing 2 wt%, 4 wt%, and 6 wt% concentrations of ammonium molybdate were meticulously introduced at a controlled pace into a precursor solution composed of 0.1 M NH_4VO_3. This process led to the formation of MoO_3/V_2O_5 nanocomposites. The thoroughly blended solutions underwent continuous stirring for a duration of one hour, followed by a brief exposure to microwave irradiation for 10 min. Subsequently, the microwave-irradiated solutions were allowed to settle undisturbed, forming a distinct and transparent precipitate.

. The obtained precipitates were subjected to multiple washes using ethanol to dissolve any remaining residues. Subsequently, the washed precipitates were dried on a hot plate. The resulting dried powders were then heated in a muffle furnace at a temperature of 200 °C for a duration of 4 h. The resulting products were labeled as follows: (a) denoting pure V_2O_5, (b) representing the 2 wt% MoO_3 loaded V_2O_5 sample, (c) indicating the 4 wt% MoO_3 loaded V_2O_5 sample, and (d) representing the 6 wt% MoO_3 loaded V_2O_5 sample.

2.2 Characterization techniques

The crystal structure analysis was conducted using PANalytical X'pert Pro X-ray diffraction (XRD) equipment. The surface morphology was examined through scanning electron microscopy (SEM) using a Vega 3 model and field emission scanning electron microscopy (FESEM) using a Zeiss model. The presence of elements was determined using energy-dispersive X-ray spectroscopy (EDAX) with an Oxford Instruments model. Fourier Transform Infrared Spectroscopy (FTIR) was employed to identify functional

Table 1 Comparative study of V_2O_5

S.No	Electrode material	Synthesis method	Electrolyte	Specific capacitance	Reference
1	V_2O_5/rGO nanocomposite	One-pot hydrothermal	3 M KOH	686.4 F g^{-1} (10 mV s^{-1}); 588.9 F g^{-1} (1 A g^{-1})	(Ahmad Shah et al., 2026) [18]
2	$Ti_3C_2T_x$@V_2O_5 composite	Microwave-assisted MXene + hydrothermal V_2O_5 + sonication	3 M KOH	1090 F g^{-1} (1 A g^{-1})	(Mashangva et al., 2026) [19]
3	V_2O_5/CNT composite	Hydrothermal	1 M Na_2SO_4	704 F g^{-1} (1 mV s^{-1}); 691 F g^{-1} (1 A g^{-1})	(Hussain et al., 2026) [20]
4	RuO_2–V_2O_5 nanocomposite	Controlled spray pyrolysis	6 M KOH	1223.48 F g^{-1} (0.1 A g^{-1})	(Liu et al., 2026) [21]
5	Te@V_2O_5 porous electrode	Salt-templating + electrochemical Te plating	PVA-LiCl gel	297 F g^{-1}	(Velmurugan et al., 2026) [22]
6	V_2O_5 nanoparticles	Microwave synthesis		499.14 F g^{-1} (2 A g^{-1})	(Alshammari, 2026) [23]
7	MXene/V_2O_5/CuNi-MOF composite	Hybrid assembly of MXene, V_2O_5 nanorods and CuNi-MOF	PVA/H_2SO_4 gel	1614 F g^{-1}	(Ghazal et al., 2026) [24]
8	Sm^{3+}-doped V_2O_5 nanoparticles	Bio-fueled solution combustion		332.28 F g^{-1}	(Ganesh et al., 2025) [25]
9	V_2O_5/TiO_2/SnO_2 ternary composite	Hydrothermal		892 F g^{-1} (1 A g^{-1})	(Steena et al., 2026) [26]
10	V_2O_5@$MnCo_2O_4$ nanocomposite	Hydrothermal + co-precipitation		428 F g^{-1} (1 A g^{-1})	(Doraswamy et al., 2026) [27]
11	V_2O_5/$Ti_3C_2T_x$ MXene hybrid	In-situ hydrothermal growth on Ni foam		798 C g^{-1} (specific capacity)	(Kumar P P & Thomas, 2026) [28]
12	V_2O_5/rGO/$Ti_3C_2T_x$ MXene nanohybrid	Nanohybrid self-assembly/integration	1 M KOH	1400 F g^{-1} (1 A g^{-1})	(Jenet et al., 2026) [29]
13	V_2O_5/CeO_2 nanocomposite	Egg albumin-assisted green synthesis		1173.05 F g^{-1} (1 A g^{-1})	(Sutharthani et al., 2026) [30]
14	MoS_2/Bi_2Se_3/V_2O_5 nanocomposite	Sol-gel auto-combustion		1469 F g^{-1} (4.5 A g^{-1})	(Mohamed Ismail et al., 2023) [31]
15	V_2O_5–$VOPO_4$ heterostructure	Combustion synthesis		310.9 mF cm^{-2}	(Prakash et al., 2026) [32]

groups using a Spectrum RX I model by Perkin Elmer. The band gap values were measured using a Lambda-35 instrument by Perkin Elmer.

The surface area and pore size were determined via BET analysis using an Autosorb iQ Station. Electrochemical investigations, including cyclic voltammetry (CV), galvanostatic charge/discharge analysis, and electrochemical impedance spectroscopy (EIS), were carried out using a BioLogic SP-300 electrochemical workstation. The working electrodes were prepared by mixing 80 wt% MoO_3/V_2O_5 nanocomposite, 15 wt% super P carbon and 5 wt% PVDF binder, with the addition of a few drops of ethanol. The resulting slurry was coated onto graphite foil and dried in a hot air oven to obtain the working electrode material. Electrochemical analysis was conducted at room temperature using a 1M H_2SO_4 and 3.5 M KOH electrolyte for the electrochemical supercapacitor studies.

Specific capacitance of the electrode materials was determined from cyclic voltammetry (CV) curves with:

$C_{sp} = \frac{\int I(V)dV}{2m \times \nu \times \Delta V}$ where C_{sp} is the specific capacitance (F/g), $\int I(V)/dV$ is the integrated area of the CV curve, m is the mass of active material (g), ν is the scan rate (V/s), and ΔV is the potential window (V).

The specific capacitance was calculated from galvanostatic charge-discharge (GCD) measurement and the following equation was used:

$C_{sp} = \frac{I\Delta t}{m\Delta V}$ where I is the discharge current (A), Δt is the discharge time (s), m is the mass of the active material (g), and ΔV is the potential window during discharge (V).

3 Result and discussion

XRD pattern of as-prepared MoO_3/V_2O_5 nanocomposites was shown in Fig. 1. The diffraction peaks showed the characteristics peaks of V_2O_5 nanostructure at (200), (100), (101), (110), (301), (314), (002), (412), (020), and (321) which corresponded to orthorhombic phase structure (JCPDS card no: 41-1426). The high crystalline nature was substantiated by the presence of intense peaks at the coordinates (100), (110), (301), (020), and (321) [33, 34]. The characteristic peaks of (110), (040), (021), (060), (002), and (042) are coined with orthorhombic phase (JCPDS card no:05-0508) of MoO_3 [35], which confirmed the presence of MoO_3 with V_2O_5. In addition, the XRD pattern revealed the emergence of hybridised MoO_3/V_2O_5 nanocomposites by displaying a mixed state of V_2O_5 and MoO_3 structure without any additional impurities [36]. The Debye-Sherrer formula was used to determine the crystallinity of the pure V_2O_5 and MoO_3 loaded (2,4,6 wt%) nanostructure's and crystalline size was calculated as ± 14 nm, + 17 nm, + 19 nm and + 20 nm respectively. and the average crystalline size of MoO_3/V_2O_5 nanocomposites was estimated as ± 18.66 nm, respectively. The results indicates that MoO_3 loading largely preserved the orthorhombic structure of V_2O_5. Minor shifts of selected diffraction peaks have been discussed by detailed examination of the diffraction patterns here in terms of lattice distortion and interfacial strain, which are caused from the interaction between the MoO_3 and V_2O_5 phases. Furthermore, the X-ray diffraction peaks of characteristic orthorhombic V_2O_5 and orthorhombic MoO_3 further validate the formation of a heterostructured composite instead of a complete replacement of Mo ions in the V_2O_5 lattice.

The FTIR spectra of the pure V_2O_5 and the MoO_3 loaded V_2O_5 nanocomposites are shown in Fig. 2. The V–O–V bending vibrations at ~ 467 cm^{-1}, V–O–V stretching vibrations at ~ 606 cm^{-1} and terminal V = O stretching vibrations at ~ 1024 cm^{-1} are assigned to the triply coordinated oxygen, doubly coordinated oxygen and terminal V = O, respectively [37, 38]. The wide absorption band at 3443 cm^{-1} is the result of the stretching vibration of hydroxyl groups on the surface and physically bound water molecules. The bands in the region of 476–823 cm^{-1} are characteristic bands which indicate that the orthorhombic V_2O_5 framework has been formed.

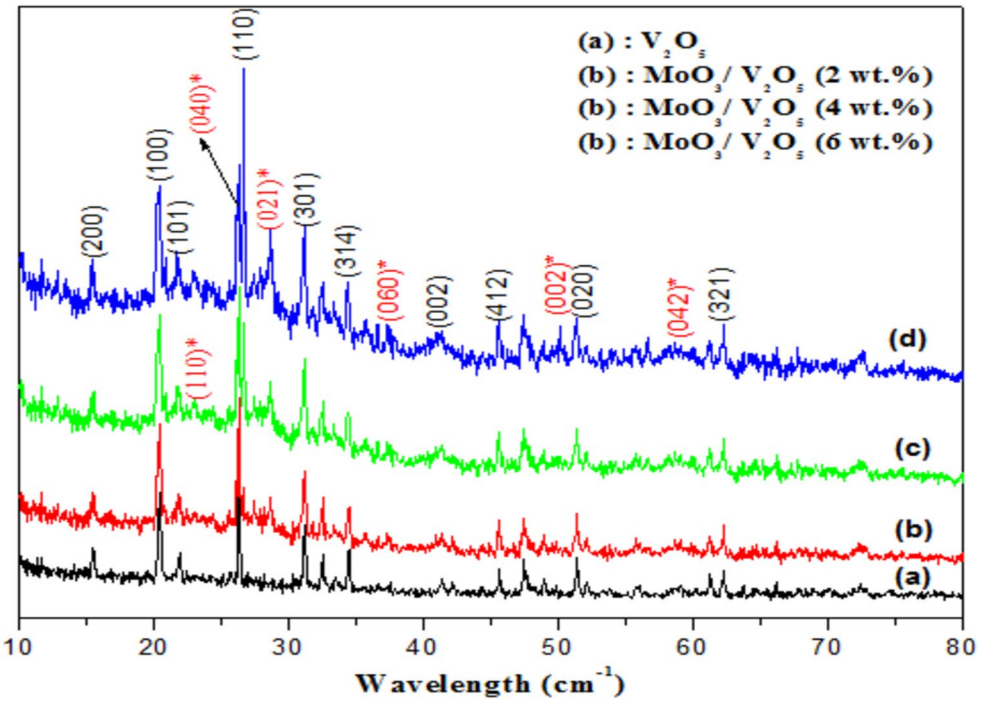


Fig. 1 XRD patterns of V_2O_5 (**a**) and MoO_3 loaded V_2O_5 (**b**, **c**,**d**) nanocomposite

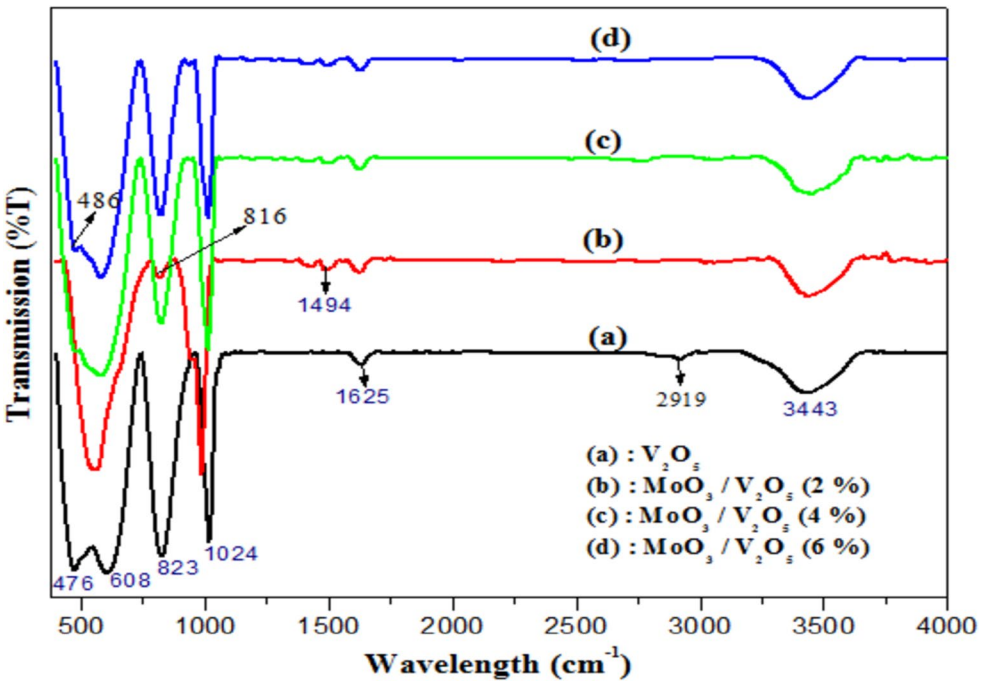


Fig. 2 FTIR spectrum of V_2O_5 (**a**) and MoO_3 loaded V_2O_5 (**b**, **c**, **d**) nanocomposite

When MoO_3 is incorporated, the following changes can be seen in the vibrational spectra: broadening of the peaks and shifting of the characteristic band from around 823 cm^{-1} to 932 cm^{-1}. The origins of this shift can be understood through the strong interfacial interaction between MoO_3 and V_2O_5, which alters the local bonding environment, and causes a lattice distortion of V_2O_5 structure [39]. The force constant of the metal–oxygen bonds changes upon incorporation of species containing Mo, causing the frequency of the vibrations to change. Moreover, the bands have increased in intensity and spread around the 755–1087 cm^{-1} region, which are related to the Mo–O stretching vibration of orthorhombic MoO_3. These observations validate the successful development of the MoO_3/V_2O_5 heterostructure and suggest electronic coupling between the two oxide phases. These observed peak shifts and peak broadening with the introduction of MoO_3 into the structure is therefore a characteristic of interfacial coupling and structural modification, not just physical mixing of the constituent oxides [40].

The structural and morphological analysis of microwave-assisted pure V_2O_5 (labeled as (a)) and MoO_3/V_2O_5 nanocomposites (labeled as (b-d)) was conducted using SEM image analysis and presented in Fig. (3). The SEM images showed the lamellar shape V_2O_5 nanostructure. When the loading ratio of MoO_3 with V_2O_5 was increased gradually, the surface of the V_2O_5 nanostructure was changed to a rod shape. To get more precise information about MoO_3/V_2O_5 (b-d) nanocomposites, FESEM image analysis was requested. FESEM analysis allows for visualization of the surface of nanostructures at very high magnifications, with resolutions ranging from a few nanometers to sub-angstrom levels. This technique is beneficial for characterizing the morphology and size of nanomaterials and studying their structure, composition, and surface chemistry. The FESEM micrographs demonstrated that the lamellar shape was modified to a nanorod shape (Fig. 4). This structure and morphology modification was attributed to the hotspot generation owing to microwave irradiation heat treatment during crystal formation. The hotspots dynamically stimulate mass transport and directional fusion into rod-shaped arranged superstructures [41]. Average length and diameter of nanorods were be estimated from the FESEM images using several representative particles. The results show that the length of the nanorods are around 300–700 nm and the diameters are 90–180 nm, depending on composition, with MoO_3 loaded V_2O_5 nanorods. The size distribution histogram, which shows the uniformity of the nanorod morphology (Fig. 5). The narrow size distribution observed is a good indication of the uniformity of the growth conditions in microwave-assisted synthesis. These other analyses give more quantitative insight into the morphology and how it affects the electrochemical performance.

The presence of Mo and V elements in the as-prepared nanostructures was examined using energy-dispersive X-ray spectroscopy (EDAX) spectrum analysis, as shown in Fig. 6. The obtained EDAX spectrum clearly showed the existence of Mo and V compounds in all samples, and the V element was rich in composition. Further, the elemental mapping analysis confirmed the same presence, as shown in Fig. 7).

Figure 8 shows the UV-Vis absorption spectra of the as-prepared nanostructures. The optical band gap was

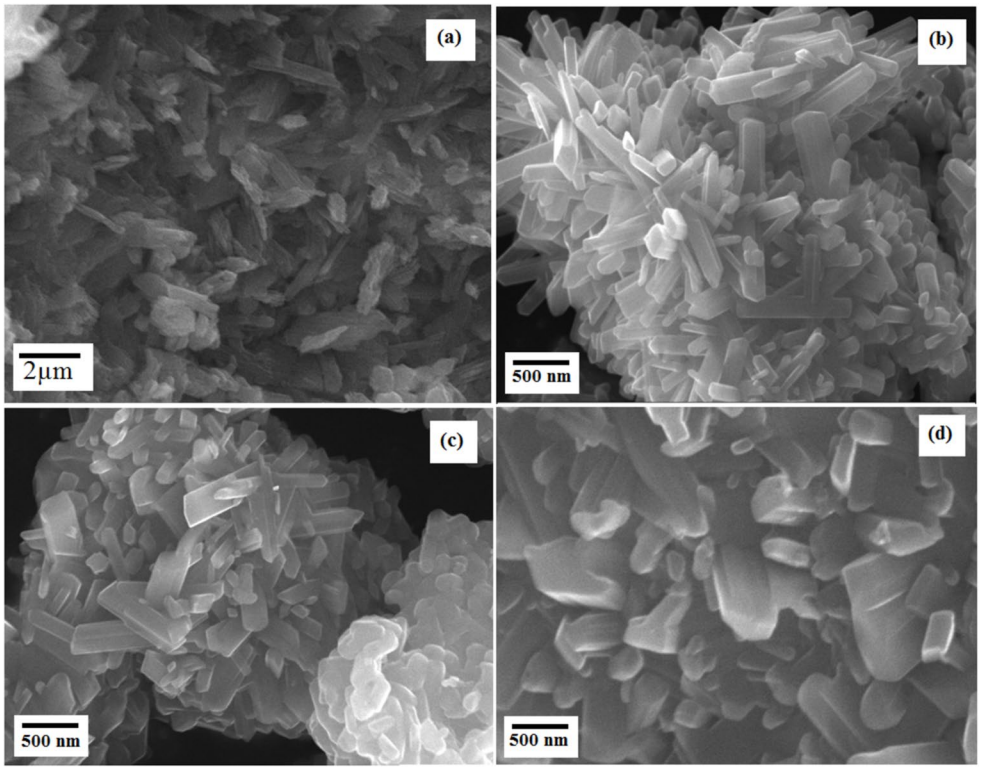


Fig. 3 SEM images of pure V_2O_5 (**a**) and MoO_3/V_2O_5 (**b-d**) nanocomposites

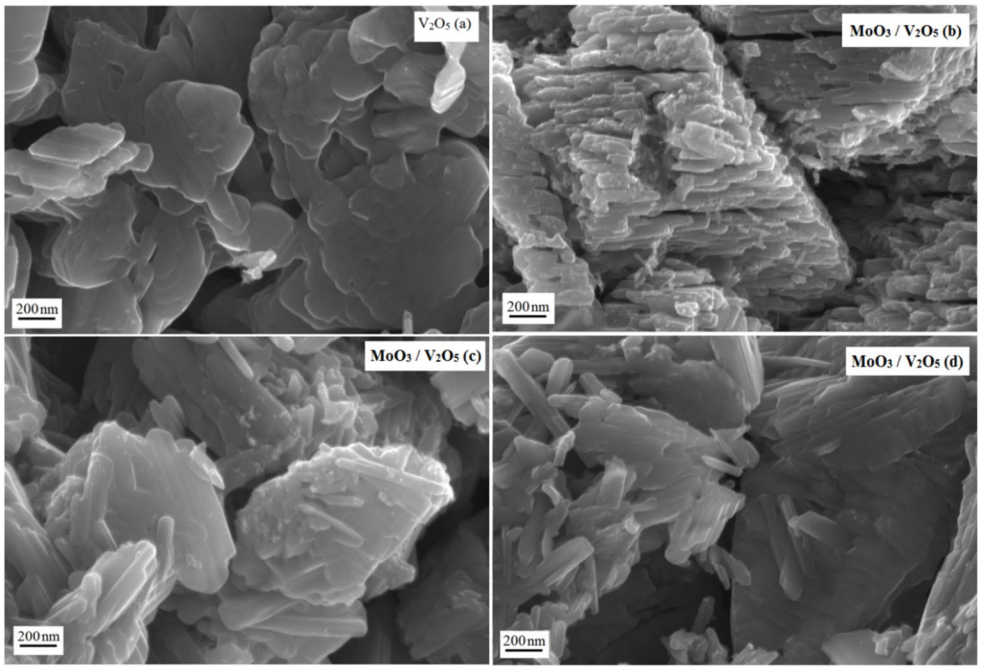


Fig. 4 FESEM images of pure V_2O_5 (**a**) and MoO_3/V_2O_5 (**b-d**) nanocomposites

calculated by the relation 1242/λ, Where λ is absorption frequency. The reflectance spectrum dramatically shifted when MoO_3 was added to the V_2O_5 crystalline structure. From the calculation, pure V_2O_5 nanostructure showed a band gap value of 3.12 eV, and adding MoO_3 with V_2O_5 nanostructure enhanced the optical band gap value to 3.15 eV, 3.17 eV, and 3.20 eV, respectively. The observed enhancement in the optical band gap is attributed to the limitation imposed by the particle size of the nanostructures.

BET analysis was conducted to estimate the particle and pore size (Fig. 9). The BET analysis demonstrated the IV-type isotherm. The surface area of the MoO_3 / V_2O_5 composite was calculated as 53.009 m^2/g. The as-synthesized nanocomposites' pore volume and radius were determined

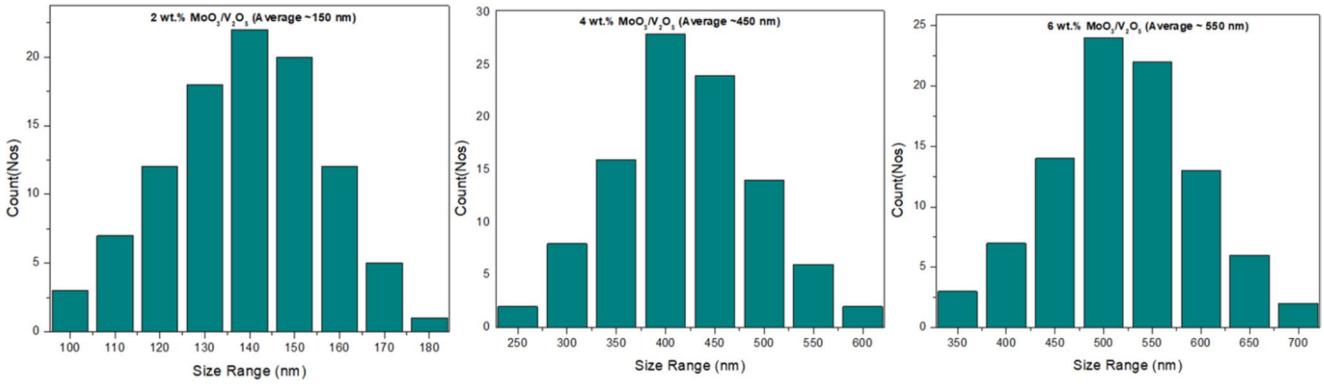


Fig. 5 Histogram calculation of MoO_3/V_2O_5 (b-d) nanocomposites

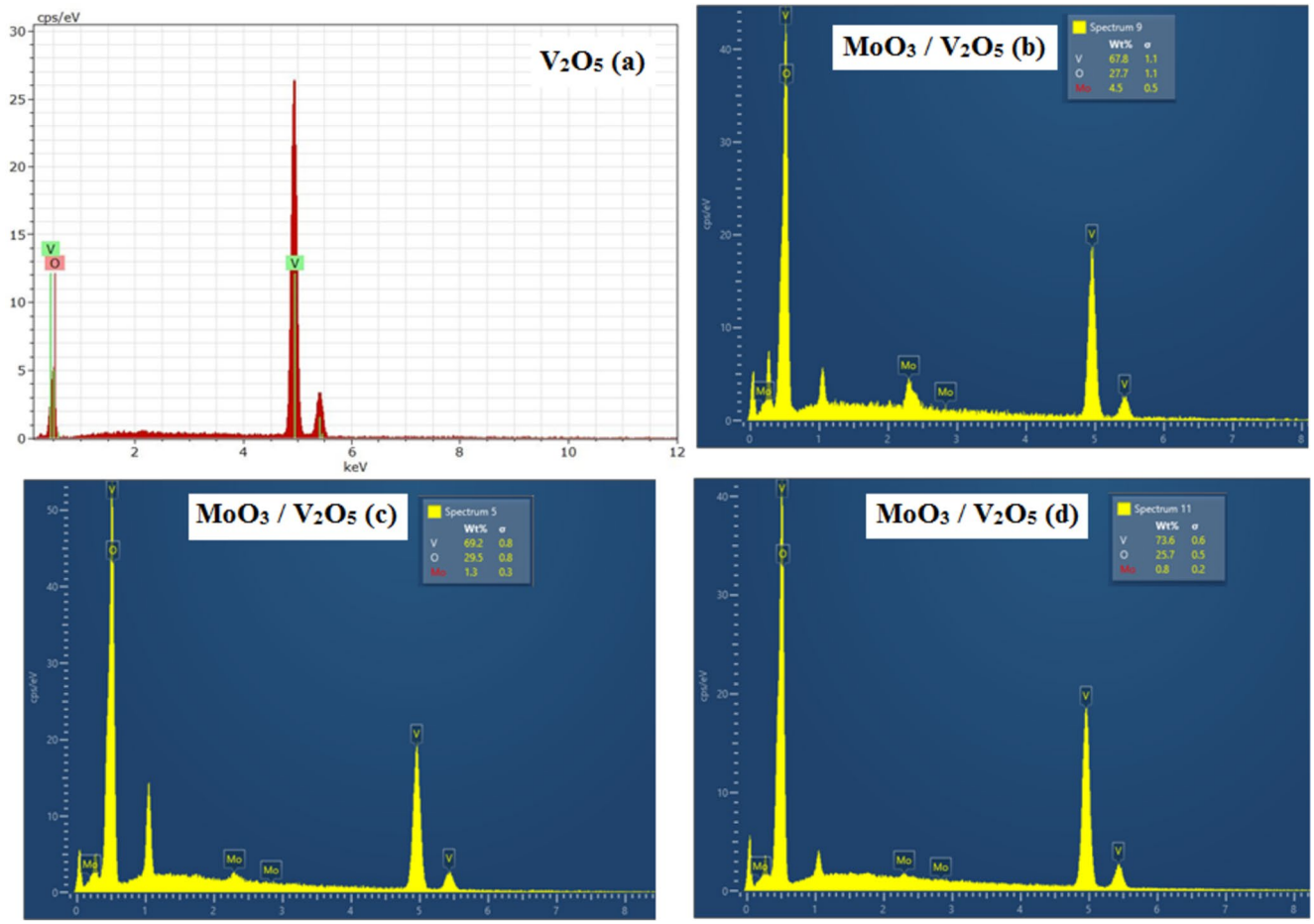


Fig. 6 EDAX spectrum of pure V_2O_5 (**a**) and MoO_3/V_2O_5 (**b-d**) nanocomposites

from BJH adsorption as 0.101 cc/g and 15.268 Å. when subject to increased pressure; the WO_3/V_2O_5 nanocomposite exhibited a sharp variation in the relative pressure isotherm, attributed to the capillary escalation occurring within the homogeneous interlayer spacing. This increase in pressure was observed in the P/P0 curve, indicating a rise in the relative pressure isotherm.

The electrochemical investigation of the as-prepared samples was conducted using a three-electrode system in 1M H_2SO_4 and 3.5 M KOH electrolytes. Cyclic voltammograms of pure V_2O_5 and MoO_3-loaded V_2O_5 nanocomposites show different redox peaks at various scan rates, which is indicative of pseudocapacitive behavior of electrodes. The reversible Faradaic reactions of the V^{5+}/V^{4+} and Mo^{6+}/Mo^{5+}

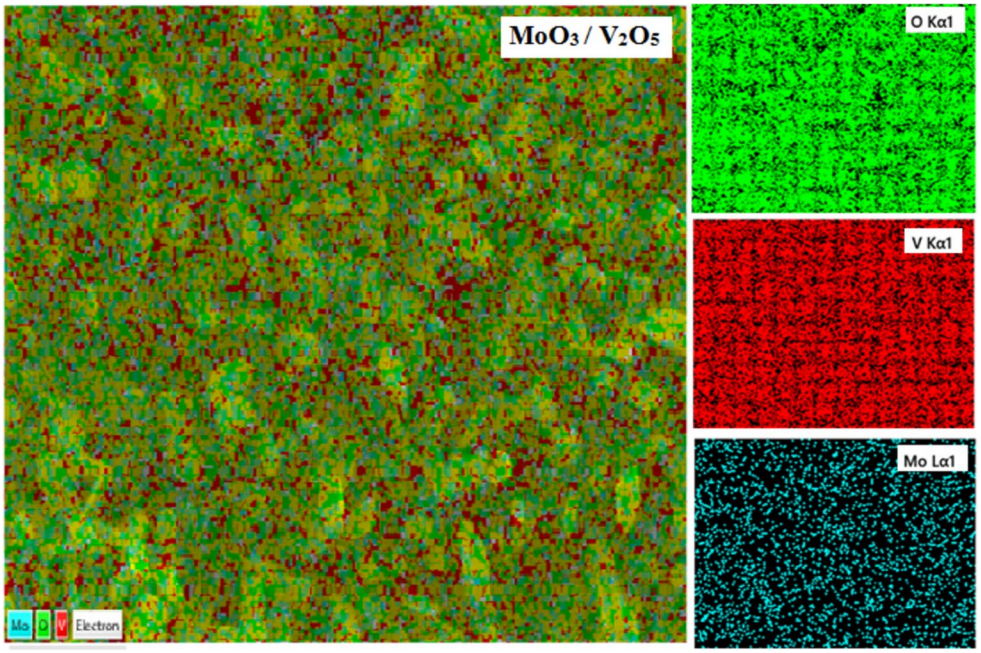


Fig. 7 Elemental Mapping Analysis

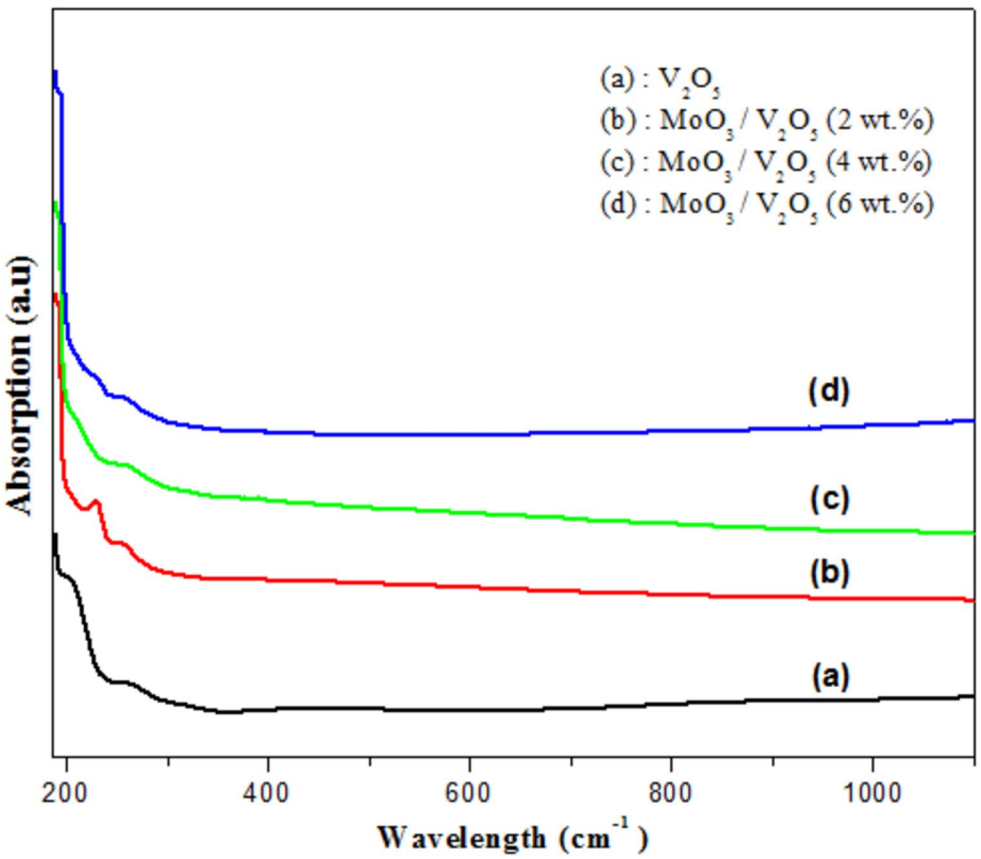


Fig. 8 UV-Vis analysis of MoO3 /V2O5

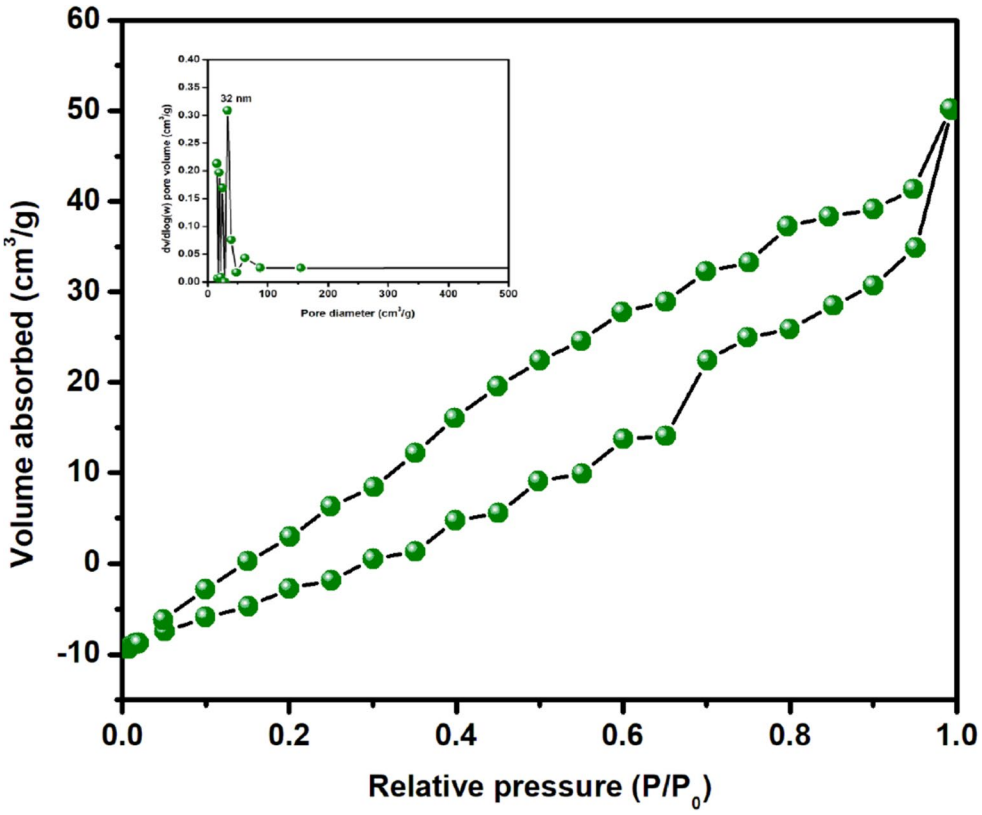


Fig. 9 BET analysis of MoO_3 / V_2O_5

redox couples are associated with the anodic and cathodic peaks observed. The current response and enclosed CV size of the device are greatly improved with the addition of MoO_3, suggesting that the device stores a greater charge. The integrated area of the nanocomposite with 6 wt% MoO_3/V_2O_5 is the highest among the investigated samples, thus showing the highest electrochemical activity.

The charge storage mechanism is based on the reversible proton insertion/extraction process in the acidic electrolyte and hydroxyl ion adsorption/desorption process in the alkaline electrolyte. The specific capacitance of as-prepared nanocomposites demonstrated as 184, 202 and 224 F/g at the current density of 1 A/g in acidic electrolyte (1M H_2SO_4) medium (Fig. 10). The same electrode materials were investigated in a 3.5 M KOH electrolyte medium and observed the maximum capacitance of 147 F/g, 159 F/g, and 172 F/g, respectively (Fig. 11). The specific energy was calculated as 31.1Wh/Kg and Specific energy density as 170 W/Kg. The enhanced electrochemical performance of the MoO_3/V_2O_5 electrode is attributed to the synergistic interaction between MoO_3 and V_2O_5. The MoO_3 phase provides additional electroactive sites and facilitates electron transport across the heterointerface, while the nanorod morphology offers shorter ion diffusion pathways and improved electrolyte accessibility. Consequently, rapid charge transfer occurs at the electrode–electrolyte interface, resulting in higher capacitance and improved rate capability.

At higher current densities, there was a gradual decrease in voltage because of the increased resistance of the electrode/electrolyte interface [2, 15]. This is owing to the resistance increasing as the current density increases. Because of this voltage drop, the potential difference between the electrodes may narrow, reducing the amount of charge that can be stored. As the scan rate increases, the peak current increases while the specific capacitance gradually decreases. This behavior is attributed to insufficient time for electrolyte ions to diffuse into the inner electroactive sites at high scan rates. At lower scan rates, the electrolyte ions can effectively penetrate the porous structure and participate in complete Faradaic reactions, leading to higher capacitance values. The minimal shift in peak potentials with increasing scan rate indicates good electrochemical reversibility and fast charge-transfer kinetics of the MoO_3/V_2O_5 heterostructure. High current densities can also cause localized heating and

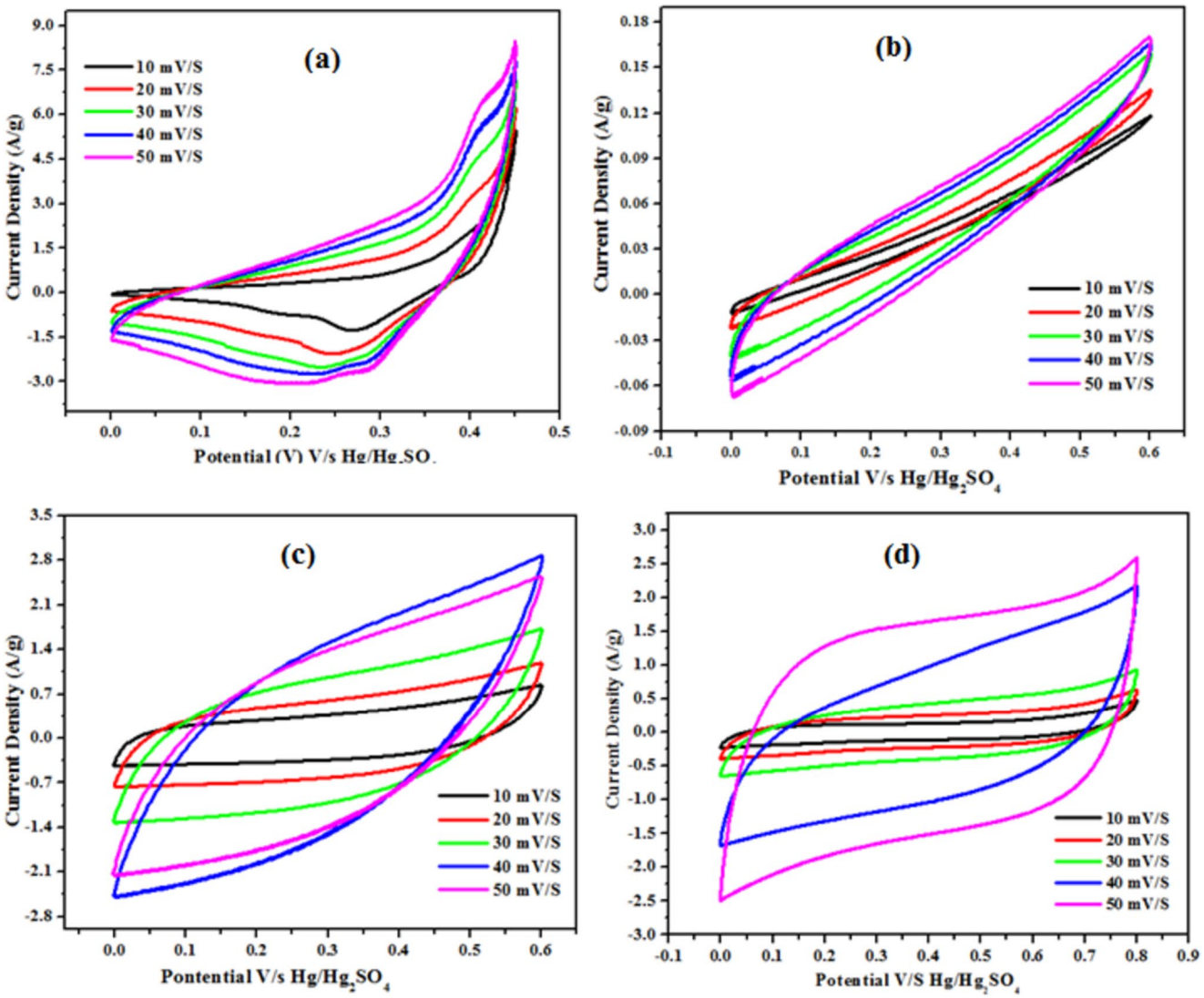


Fig. 10 Cyclic voltagram in 1M H_2SO_4 electrolyte of V_2O_5 (**a**) and MoO_3 / V_2O_5 (**b-d**)

stress within the electrode, which can further contribute to material degradation and inefficient consumption [42].

The charge-discharge analysis for the as-prepared electrodes was conducted in both electrolytes (1 M H_2SO_4 and 3.5 M KOH) and depicted in Figs. 12 and 13. The galvanostatic charge and discharge curves of the nanocomposites MoO_3/V_2O_5 show non-linear charge and discharge curves, which further indicates that the electrode material has a pseudocapacitive property. The deviation from an ideal tripod shape suggests that there are Faradaic redox reactions on top of the charge storage in the electric double layer.

The optimized 6 wt% MoO_3/V_2O_5 electrode has the longest discharge duration, that is, its highest specific capacitance. An extended discharge time means efficient use of electroactive sites and better ion diffusion in the structure of the electrode. The enhanced electrochemical properties are believed to be due to the presence of MoO_3/V_2O_5 hetero-interfaces that can accelerate electron transport and decrease the charge transfer resistance. In the charging process, electrolyte ions migrate from the bulk electrolyte to the electrode surface, and enter reversible redox reactions of vanadium and molybdenum species. On discharge, the

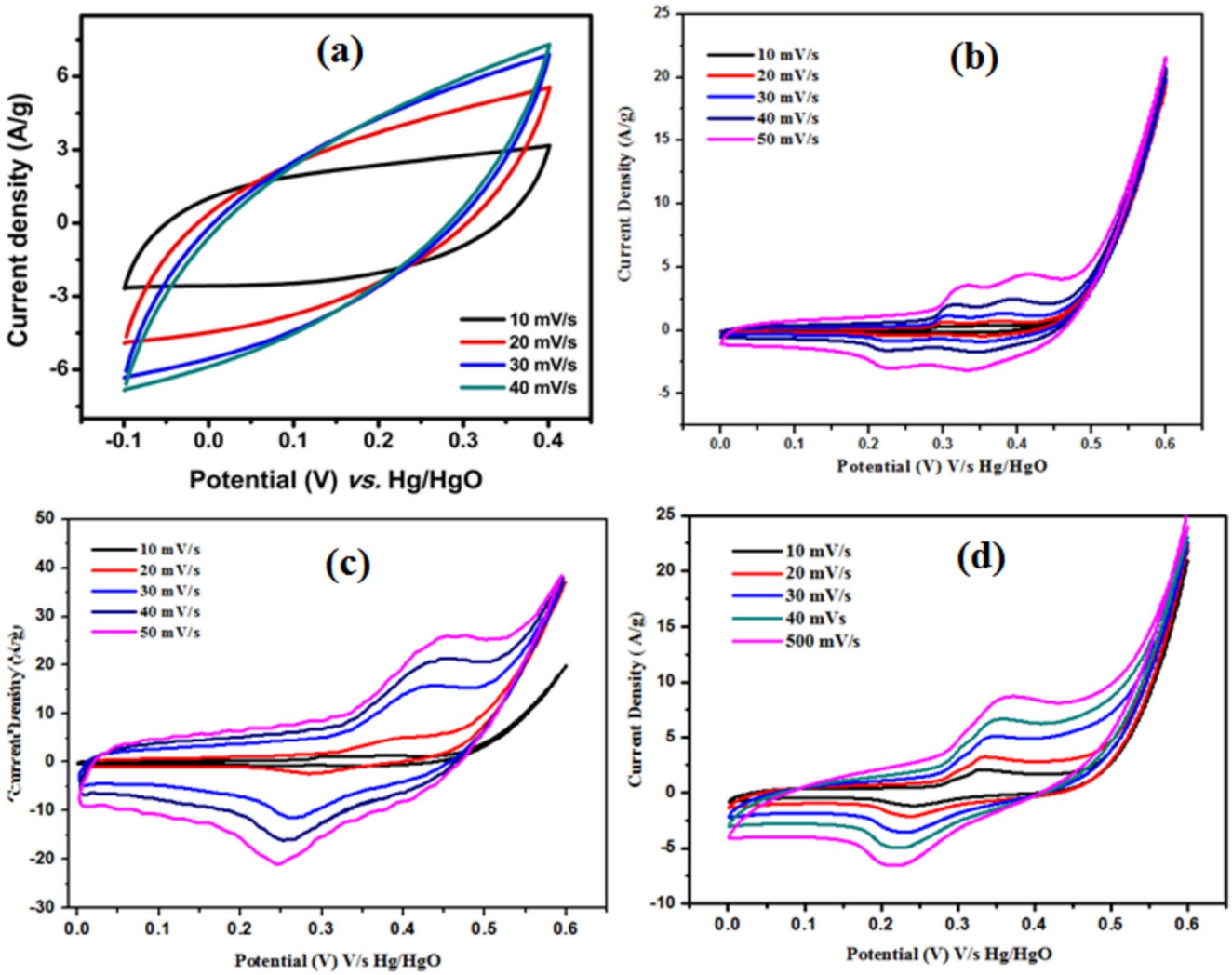


Fig. 11 Cyclic voltagram in 3.5 KOH electrolyte of V_2O_5 (**a**) and MoO_3 / V_2O_5 (**b-d**)

stored charge is discharged via the reverse reactions, thus providing a prolonged discharge performance. The low internal resistance as indicated by the IR drop at the starting point of the discharge curve indicates that the internal resistance is low and the electrical conductivity properties are good. The discharge time becomes shorter and the specific capacitance decreases with an increase of the applied current density. This is explained by the fact that at higher current densities, only the outer electroactive sites are involved in the charge storage process and the ion diffusion of the electrolyte is limited. However, high values of capacitance that remain even at high current density indicate good rate capability and charge transport efficiency of the MoO_3/V_2O_5 nanostructure. The better electrochemical performance of the optimized electrode is therefore explained by the following: (i) the higher electrical conductivity is thanks to the incorporation of MoO_3, (ii) the higher electrochemically active surface area is due to the formation of nanorods, (iii) the shorter ion diffusion pathways and (iv) the synergistic redox activity shown by the coexistence of V^{5+}/V^{4+} and Mo^{6+}/Mo^{5+} redox couples [2, 15].

It signifies that the supercapacitor exhibits efficient charge transfer kinetics and maintains a high Coulombic efficiency, enabling reliable and sustainable energy storage over

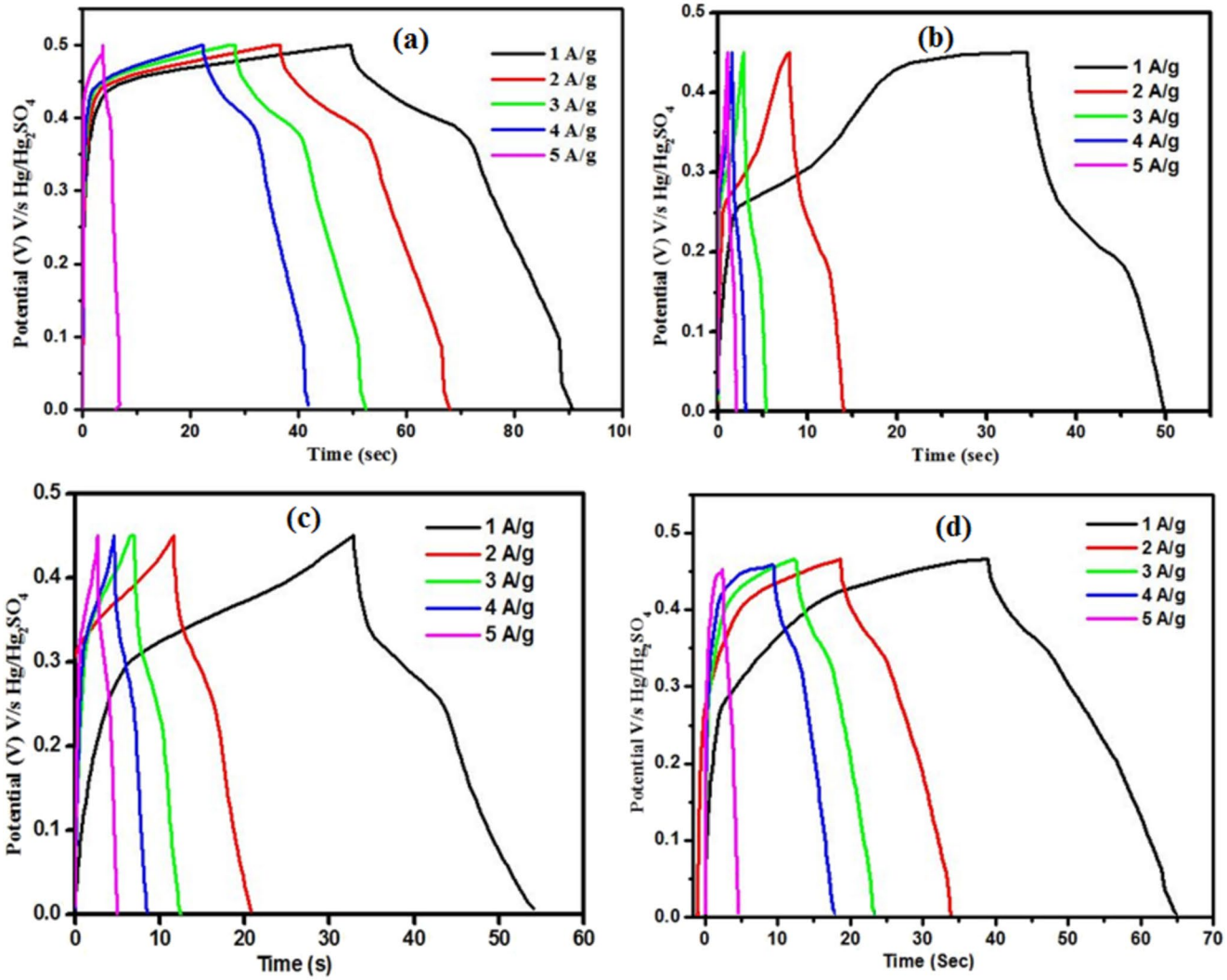


Fig. 12 GCD in H_2SO_4 electrolyte of V_2O_5 (**a**) and MoO_3 / V_2O_5 (**b-d**)

numerous charge-discharge cycles. The charge-discharge time progressively decreases as the current density increases and the specific capacity diminishes. The elevation of current density induces a significant uptake of vanadium electrolyte ions at the electrode interface, causing a rapid reduction in vanadium ion concentration at the interface. This decline in concentration triggers an increase in concentration polarization. Sustaining a high current density necessitates higher excitation voltage, yet it does not increase the charge at the interface. Consequently, this circumstance decreases specific capacitance as the current density rises [43, 44].

The EIS spectra of the as-prepared electrode material was shown in Fig. 14. An Ultracapacitor is a circuit assembly comprising numerous interconnected capacitors and resistors. With an increase in test frequency, the influence of resistor R becomes more prominent. In contrast, a decrease in frequency leads to a more significant impact on capacitor C. At the same time, primarily determine the impedance Z in the low-frequency region (LF), the impedance Z is characterized by the series combination of resistance R and capacitance C. EIS measurement reveals a high-frequency resistance of 2.84 Ω.

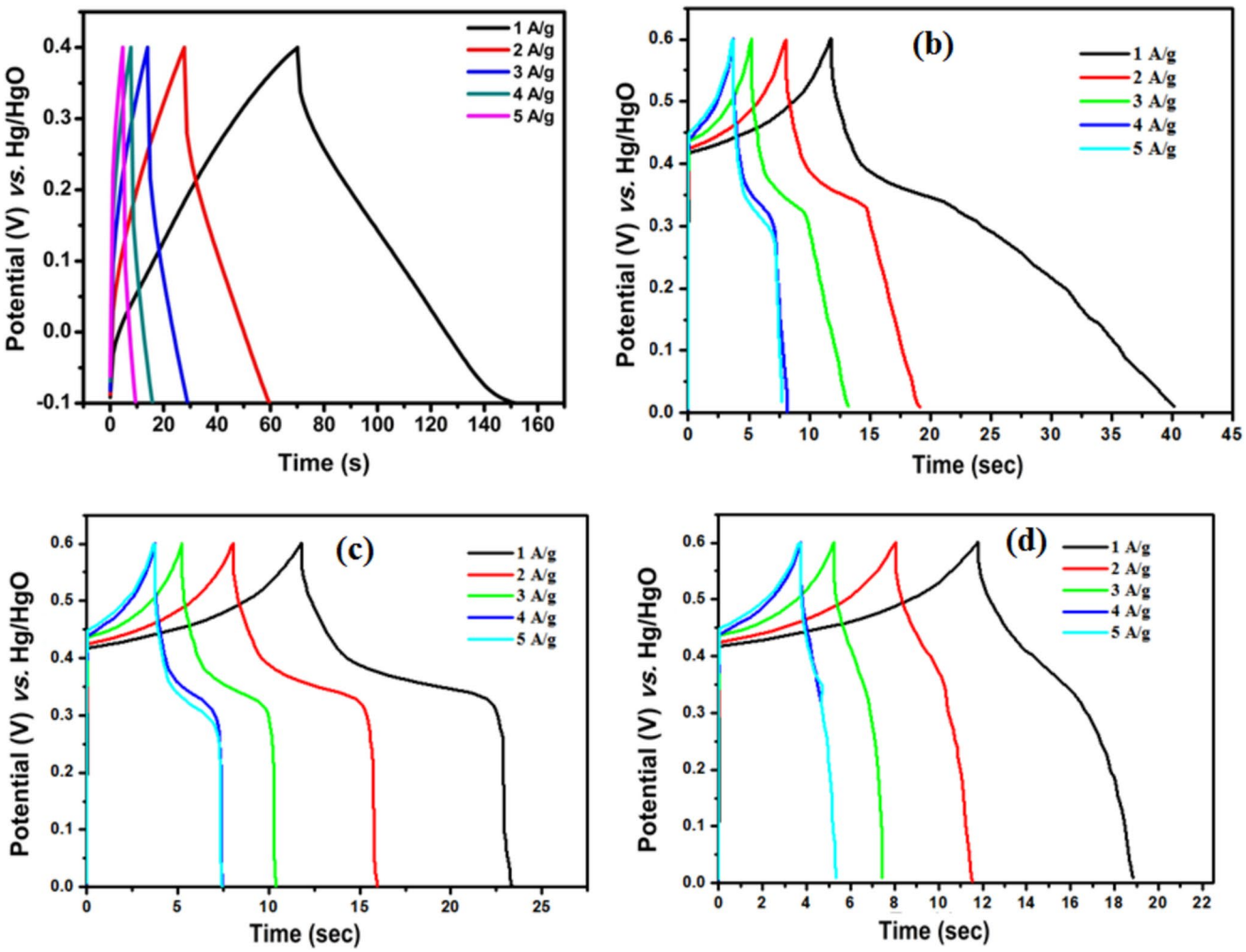


Fig. 13 GCD Curves in 3.5 M KOH electrolyte of V_2O_5 (**a**) and MoO_3 / V_2O_5 (**b-d**)

Additionally, the semicircle was observed in the low-frequency region is higher, indicating a more rapid diffusion rate of ions. This enhanced ion diffusion rate contributes to the supercapacitor's improved charge and discharge rate [45]. Figure 15 demonstrated the long cycle performance and indicated that the as-prepared electrode was stable up to 5000 cycles with a capacitance retention of 71%. Supercapacitors primarily utilize Faraday reactions for energy storage, and it is known that the fast reversible redox reactions involved in these processes are not entirely reversible in experimental conditions. Consequently, a decline in specific capacitance often occurs during cycle testing. The electrode material's structural integrity and electrochemical reaction heavily influence supercapacitors' cycling performance. Addressing the structural instability of V_2O_5 can be achieved by constructing distinctive nanostructures, which can mitigate degradation and enhance the cycling stability of the supercapacitor system [46].

4 Conclusion

In this study, MoO_3/V_2O_5 nanocomposites were synthesized using a microwave-assisted method. The X-ray diffraction (XRD) analysis confirmed the presence of characteristic peaks corresponding to the orthorhombic phase of V_2O_5

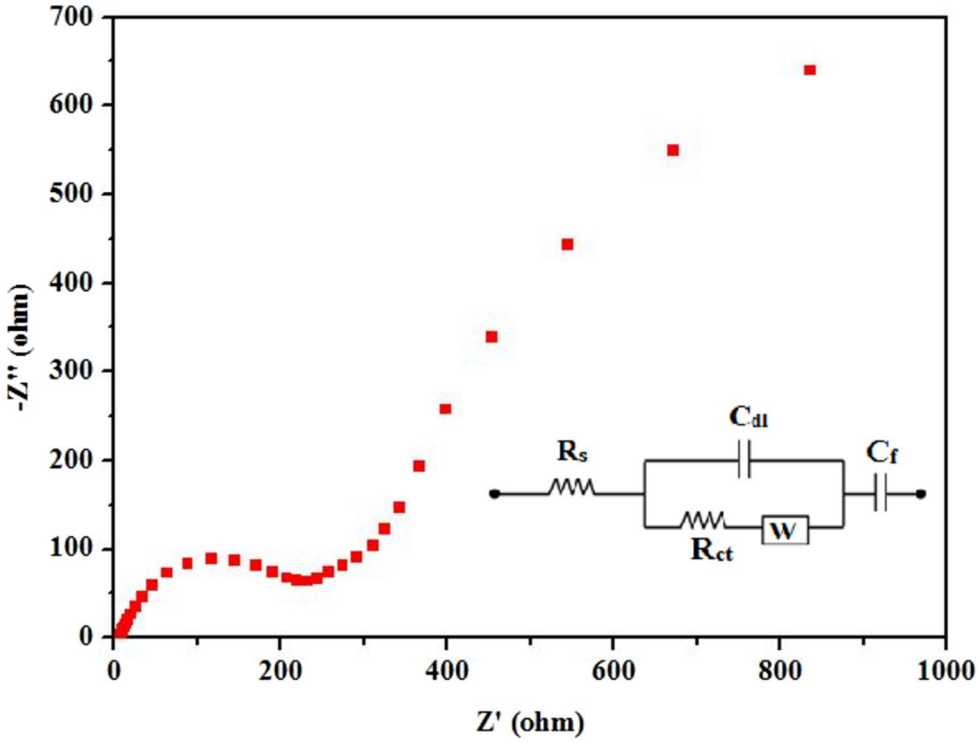


Fig. 14 Electrochemical Impedance spectra of MoO_3 / V_2O_5

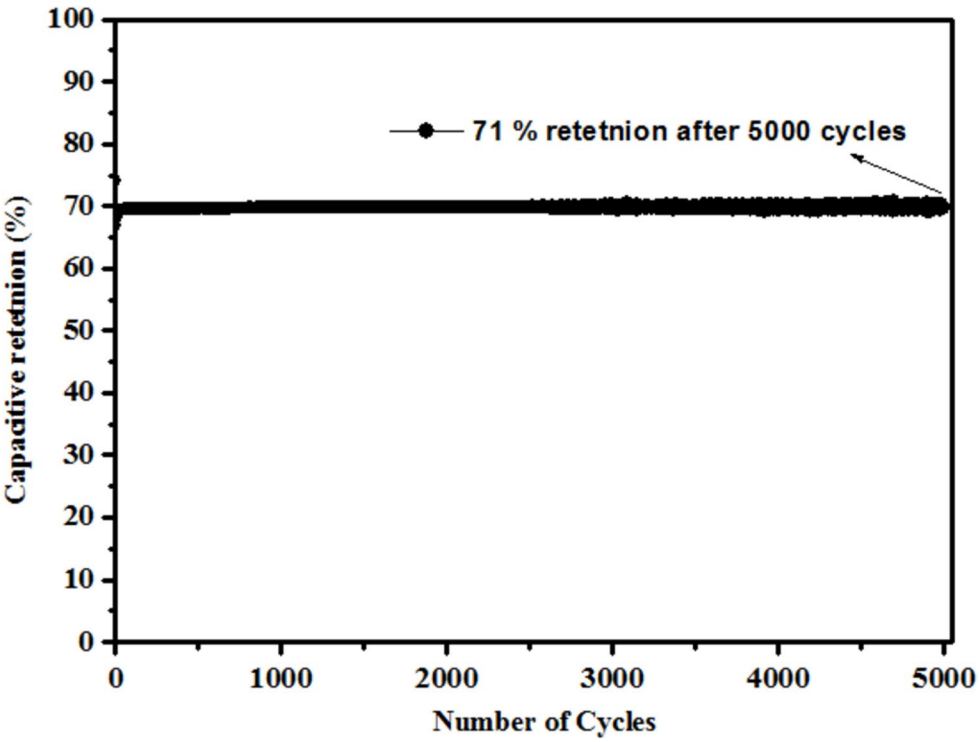


Fig. 15 Long Cycle Test

nanostructures, along with the presence of MoO_3. Fourier Transform Infrared Spectroscopy (FTIR) identified various functional groups in the nanocomposites. Scanning Electron Microscopy (SEM) images revealed the lamellar shape of the V_2O_5 nanostructures. However, Field Emission Scanning Electron Microscopy (FESEM) showed a modification of the lamellar shape into a nanorod shape. Energy-dispersive X-ray spectroscopy (EDAX) analysis confirmed the presence of Mo and V elements in the prepared nanostructures. The specific capacitance of the as-prepared nanocomposites was determined to be 184 F/g, 202 F/g, and 224 F/g at a current density of 1 A/g in the acidic electrolyte (1M H_2SO_4). When tested in

a 3.5 M KOH electrolyte medium, the maximum capacitance values observed were 147 F/g, 159 F/g, and 172 F/g, respectively. The long-cycle performance of the electrode demonstrated good stability, as the nanocomposites retained 71% of their initial capacitance after 5000 cycles. These findings suggest the potential of the MoO_3/V_2O_5 nanocomposites for electrochemical energy storage applications.

Author contributions K.Latha conducted the experiments and wrote main manuscript. Anbuselvi supervised the experimental work and reviewed the manuscript.

Data availability No datasets were generated or analysed during the current study.

Declarations

Competing interests The authors declare no competing interests.

References

1. B. Pal, S. Yang, S. Ramesh, V. Thangadurai, R. Jose, Electrolyte selection for supercapacitive devices: a critical review. Nanoscale Adv. **1**, 3807–3835 (2019). https://doi.org/10.1039/C9NA00374F
2. C. Liu, F. Li, M. Lai-Peng, H.M. Cheng, Advanced materials for energy storage. Adv. Mater. **22**, E28–62 (2010). https://doi.org/10.1002/adma.200903328
3. P. Periasamy, M. Chavli, Aqueous electrolytes for electrochemical supercapacitors. Electrolytes Energy Storage Appl. 271–286 (2024). https://doi.org/10.1201/9781003441182-16
4. P. Periasamy, T. Krishnakumar, M. Sandhiya, M. Sathish, M. Chavali, P.F. Siril, V.P. Devarajan, Electrochemical investigation of hybridized WO 3 –CdS semiconducting nanostructures prepared by microwave-assisted wet chemical route for supercapacitor application. J. Mater. Sci. Mater. Electron. **30**, 9231–9244 (2019). https://doi.org/10.1007/s10854-019-01252-w
5. B.E. Conway, Electrochemical behavior at porous electrodes; Applications to capacitors, electrochem. Supercapacitors (1999) 377–416. https://doi.org/10.1007/978-1-4757-3058-6_14
6. J. Li, X. Wang, Q. Huang, S. Gamboa, P.J. Sebastian, Studies on preparation and performances of carbon aerogel electrodes for the application of supercapacitor. J. Power Sources. **158**, 784–788 (2006). https://doi.org/10.1016/j.jpowsour.2005.09.045
7. F. Wang, S. Xiao, Y. Hou, C. Hu, L. Liu, Y. Wu, Electrode materials for aqueous asymmetric supercapacitors. RSC Adv. (2013). https://doi.org/10.1039/c3ra23466e
8. P. Periasamy, T. Krishnakumar, M. Sathish, M. Chavali, P.F. Siril, V.P. Devarajan, 2-D Nanostructures of Advanced Hybridized WO3 Nanocomposites for High Performance of Supercapacitor Application, Mater. Horizons From Nat. to Nanomater. (2021) 1–42. https://doi.org/10.1007/978-981-15-8307-0_1
9. P. Periasamy, M. Chavali, M.P. Nikolova, M. Bououdina, B. Selvakumar, K.S. Kannan, Green synthesis of metal oxide-based electrode materials for supercapacitor electrode, sustain. Green synth. Nano-dimensional mater. Energy Environ. Appl. 123–143 (2024). https://doi.org/10.1201/9781003362241-7/GREEN-SYNTHESIS-METAL-OXIDE-BASED-ELECTRODE-MATERIALS-SUPERCAPACITOR-ELECTRODE-PERIASAMY-MURTHY-CHAVALI-MARIA-PLAMENOVA-NIKOLOVA-MOHAMED-BOUOUDINA-SELVAKUMAR-SENTHIL-KANNAN
10. S. Lindberg, N.M. Ndiaye, N. Manyala, P. Johansson, A. Matic, A VO2 based hybrid super-capacitor utilizing a highly concentrated aqueous electrolyte for increased potential window and capacity. Electrochim. Acta. **345** (2020). https://doi.org/10.1016/j.electacta.2020.136225
11. J. Mu, J. Wang, J. Hao, P. Cao, S. Zhao, W. Zeng, B. Miao, S. Xu, Hydrothermal synthesis and electrochemical properties of V2O5 nanomaterials with different dimensions, Ceram. Int. (2015). https://doi.org/10.1016/j.ceramint.2015.06.091
12. B. Saravanakumar, K.K. Purushothaman, G. Muralidharan, MnO2 grafted V2O5 nanostructures: Formation mechanism, morphology and supercapacitive features, CrystEngComm (2014). https://doi.org/10.1039/c4ce01476f
13. A. Gaber, S.Y. Attia, A.M.S. Salem, S.G. Mohamed, S.I. El-Hout, Microwave-assisted fabrication of SnO2 nanostructures as electrode for high-performance pseudocapacitors. J. Energy Storage. **59**, 106358 (2023). https://doi.org/10.1016/J.EST.2022.106358
14. K. Latha, S. Anbuselvi, P. Periasamy, R. Sudha, D. Velmurugan, Microwave-Assisted hybridised WO3/V2O5 rod shape nanocomposites for electrochemical supercapacitor applications. Inorg. Chem. Commun. **133**, 108927 (2021). https://doi.org/10.1016/J.INOCHE.2021.108927
15. P. Simon, Y. Gogotsi, Materials for electrochemical capacitors. Nat. Mater. **7**, 845–854 (2008). https://doi.org/10.1038/NMAT2297
16. Y. Yang, D. Kim, M. Yang, P. Schmuki, Vertically aligned mixed V2O5-TiO2 nanotube arrays for supercapacitor applications. Chem. Commun. (2011). https://doi.org/10.1039/c1cc11811k
17. K. Pradeeswari, A. Venkatesan, P. Pandi, K.G. Prasad, K. Karthik, T. Maiyalagan, R.M. Kumar, Effect of cerium on electrochemical properties of V2O5 nanoparticles synthesized via non-aqueous sol-gel technique. Ionics (Kiel). (2020). https://doi.org/10.1007/s11581-019-03259-z
18. S. Ahmad Shah, O. Amin, H. Mahajan, S. Kaur, S. Jan, S. Sharma, D. Basandrai, One-pot hydrothermal Fabrication of thermally stable V2O5/rGO nanocomposite for high-rate pseudocapacitors. Ceram. Int. **52**(14), 27208–27218 (2026). https://doi.org/10.1016/J.CERAMINT.2026.04.269
19. T.T. Mashangva, N. Vishwakarma, P.P. Singh, S. Prasher, R. Dhiman, M. Kumar, A. Sharma, Synergistic enhancement of electrochemical properties in domestic microwave-assisted Ti3C2TX MXene composite with V_2O_5 nanoparticles for supercapitor applications. J. Energy Storage. **150**, 120387 (2026). https://doi.org/10.1016/J.EST.2026.120387
20. S. Hussain, Z. Miao, Y. Han, A.S. Ganie, A. Jalil, M.M. Alam, A.G. Al-Sehemi, R.K. Manavalan, X. Zhang, G. Qiao, Highly efficient V2O5@In2O3 nanoflowers for outstanding NO2 gas sensing proficiencies. Microchem. J. **223**, 117359 (2026). https://doi.org/10.1016/J.MICROC.2026.117359
21. X. Liu, C. Chen, H. Ren, Y. Long, Q. Guo, L. Yang, X. Ge, Suppressing self-discharge of vanadium based Na-supercapacitor based on conjugated device configuration. J. Energy Storage. **172**, 123010 (2026). https://doi.org/10.1016/J.EST.2026.123010
22. R. Velmurugan, A. Sakthivel, A. Chandrasekaran, B. Subramanian, J.Y. Lin, Superior rate capability of electrochemical energy storage devices utilizing ultra-thin binder-free V2O5 spherical nanostructured electrodes via pulse laser ablation approach. Surf. Interfaces. **87**, 108955 (2026). https://doi.org/10.1016/J.SURFIN.2026.108955
23. F.H. Alshammari, Structure–property correlations, optical behavior, and dielectric relaxation dynamics in V2O5/thermoplastic polyurethane nanocomposites for flexible electronic applications. Ceram. Int. **52**(1), 286–297 (2026). https://doi.org/10.1016/J.CERAMINT.2025.11.317
24. A. Ghazal, I. Kim, A.C. Mendhe, S. Dhas, A. Javed, R. Batool, D. Kim, Advanced design of 2D MXene/1D V2O5/3D CuNi MOF for stable electrochemical properties under static/dynamic

bending. J. Energy Storage. **145**, 119812 (2026). https://doi.org/10.1016/J.EST.2025.119812
25. C.U.C. Ganesh, B.R.R. Krushna, I.S. Pruthviraj, G. Ramakrishna, S.C. Sharma, A. George, S. Mishra, U. Premkumar, K. Manjunatha, S.Y. Wu, H.C. Kuo, V. Shivakumar, S. Devaraja, H. Nagabhushana, Green synthesis of Ce3+ doped V2O5 NPs as an advanced electrode material for possible supercapacitor and therapeutic applications. J. Taiwan Inst. Chem. Eng. **174**, 106223 (2025). https://doi.org/10.1016/J.JTICE.2025.106223
26. A.S. Steena, S.R. Niranjana, S. Harini, S. Prathap, K. Kaviyarasu, M.V.A. Raj, Optimization and electrochemical assessment of V2O5/TiO2/SnO2 ternary nanocomposites as efficient electrode materials for supercapacitor applications. J. Phys. Chem. Solids. **209**, 113306 (2026). https://doi.org/10.1016/J.JPCS.2025.113306
27. G. Doraswamy, K. Thejasree, G. Krishna , V., K.T. Ramakrishna Reddy, Heterointerface-engineered V2O5@MnCo2O4 nanocomposite for high-performance and durable supercapacitors. Mater. Sci. Semiconduct. Process. **214**, 110831 (2026). https://doi.org/10.1016/J.MSSP.2026.110831
28. P.P. Kumar , A., N. Thomas, In situ assembled V2O5/Ti3C2Tx MXene hybrid composite with enhanced interfacial coupling for high performance supercapacitors. J. Power Sources. **678**, 240128 (2026). https://doi.org/10.1016/J.JPOWSOUR.2026.240128
29. Jenet, J. E., Ramachandran, T., Raji, R. K., Kandhan, K., Balasubramanian, N., Suba Sri, M., Hamed, F., Subramanian, G., & Pachamuthu, M. P. (2026). Synergistic interfacial engineering of a V2O5/rGO/Ti3C2Tx MXene nanohybrid for ultrahigh supercapacitors. Materials Chemistry and Physics, 363 https://doi.org/10.1016/J.MATCHEMPHYS.2026.132779
30. K. Sutharthani, S.S. Pradeepa, R.S. Devi, M. Sivakumar, Dual role of redox-active V2O5/CeO2 nanocomposite electrodes in high-performance supercapacitor and battery applications. Adv. Powder Technol. **37**(2), 105185 (2026). https://doi.org/10.1016/J.APT.2026.105185
31. K.B. Mohamed Ismail, A. Kumar, M. Jayavel, R. Arivanandhan , M., M.A. Mohamed Ismail, Enhanced electrochemical performance of the MoS2/Bi2S3 nanocomposite-based electrode material prepared by a hydrothermal method for supercapacitor applications. RSC Adv. **13**(35), 24272–24285 (2023). https://doi.org/10.1039/D3RA03892K
32. H.C. Prakash, D. Santhanagopalan, S.K. Batabyal, Layered V2O5-VOPO4 heterostructure photo-sensitive electrodes for light-enhanced, flexible, and ultra-stable supercapacitor with 1.7 lakh cycle life. J. Energy Storage. **144**, 119663 (2026). https://doi.org/10.1016/J.EST.2025.119663
33. B. Balamuralitharan, I.H. Cho, J.S. Bak, H.J. Kim, V2O5 nanorod electrode material for enhanced electrochemical properties by a facile hydrothermal method for supercapacitor applications. New. J. Chem. (2018). https://doi.org/10.1039/c8nj02377h
34. Y. Zhang, Y. Huang, Facile synthesis and characterization of rough surface V2O5 nanomaterials for pseudo-supercapacitor electrode material with high capacitance. Bull. Mater. Sci. (2017). https://doi.org/10.1007/s12034-017-1470-5
35. M. Abinaya, K. Saravanakumar, E. Jeyabharathi, V. Muthuraj, Synthesis and characterization of 1D-MoO3 nanorods using abutilon indicum extract for the photoreduction of hexavalent chromium. J. Inorg. Organomet. Polym. Mater. **29**, 101–110 (2019). https://doi.org/10.1007/s10904-018-0970-0
36. H. Chuai, D. Zhou, X. Zhu, Z. Li, W. Huang, Characterization of V2O5/MoO3 composite photocatalysts prepared via electrospinning and their photodegradation activity for dimethyl phthalate. Cuihua Xuebao/Chinese J. Catal. **36**, 2194–2202 (2015). https://doi.org/10.1016/S1872-2067(15)61002-6
37. X. Zhou, G. Wu, J. Wu, H. Yang, J. Wang, G. Gao, R. Cai, Q. Yan, Multiwalled carbon nanotubes–V2O5 integrated composite with nanosized architecture as a cathode material for high performance lithium ion batteries. J. Mater. Chem. A **1**, 15459–15468 (2013). https://doi.org/10.1039/C3TA13143B
38. M. Farahmandjou, Chemical Synthesis of Vanadium Oxide (V2O5) Nanoparticles prepared by sodium metavanadate. J. Nanomed. Res. (2017). https://doi.org/10.15406/jnmr.2017.05.00103
39. S.K. Sen, T.C. Paul, M.S. Manir, S. Dutta, M.N. Hossain, J. Podder, Effect of Fe-doping and post annealing temperature on the structural and optical properties of MoO3 nanosheets. J. Mater. Sci. Mater. Electron. **30**, 14355–14367 (2019). https://doi.org/10.1007/s10854-019-01805-z
40. S. Kothaplamoottil Sivan, A.K.K. Padinjareveetil, V.V.T. Padil, R. Pilankatta, B. George, C. Senan, M. Černík, R.S. Varma, Greener assembling of MoO3 nanoparticles supported on gum arabic: cytotoxic effects and catalytic efficacy towards reduction of p-nitrophenol. Clean. Technol. Environ. Policy. **21**, 1549–1561 (2019). https://doi.org/10.1007/s10098-019-01726-9
41. X. Hu, J. Gong, L. Zhang, J.C. Yu, Continuous size tuning of monodisperse ZnO colloidal nanocrystal clusters by a microwave-polyol process and their application for humidity sensing. Adv. Mater. **20**, 4845–4850 (2008). https://doi.org/10.1002/ADMA.200801433
42. B.E. Conway, Electrochemical capacitors based on pseudocapacitance. electrochem. Supercapacitors. 221–257 (1999). https://doi.org/10.1007/978-1-4757-3058-6_10
43. S.A. Pande, B. Pandit, B.R. Sankapal, Vanadium oxide anchored MWCNTs nanostructure for superior symmetric electrochemical supercapacitors. Mater. Des. (2019). https://doi.org/10.1016/j.matdes.2019.107972
44. A. Mauger, C.M. Julien, V2O5 thin films for energy storage and conversion. AIMS Mater. Sci. (2018). https://doi.org/10.3934/matersci.2018.3.349
45. B.E. Conway, Electrochemical supercapacitors: scientific fundamentals and technological applications, (1999) 698
46. K. Latha, S. Anbuselvi, P. Periasamy, R. Sudha, D. Velmurugan, Structural and electrochemical investigation of novel hybridized MnO2/V2O5 nanocomposites prepared by one-step microwave-assisted method for electrochemical supercapacitor application. J. Mater. Sci. Mater. Electron. **32**, 23293–23308 (2021). https://doi.org/10.1007/S10854-021-06814-5

Publisher's note Springer Nature remains neutral with regard to jurisdictional claims in published maps and institutional affiliations.

Springer Nature or its licensor (e.g. a society or other partner) holds exclusive rights to this article under a publishing agreement with the author(s) or other rightsholder(s); author self-archiving of the accepted manuscript version of this article is solely governed by the terms of such publishing agreement and applicable law.